






Open Archive Toulouse Archive Ouverte

OATAO is an open access repository that collects the work of Toulouse researchers and makes it freely available over the web where possible

This is an author's version published in: <http://oatao.univ-toulouse.fr/23324>

Official URL : <https://doi.org/10.1016/j.ijthermalsci.2016.04.017>

To cite this version:

Baudin, Nicolas  and Colin, Catherine  and Ruyer, Pierre and Sebilleau, Julien 
Turbulent flow and transient convection in a semi-annular duct. (2016) International Journal of Thermal Sciences, 108. 40-51. ISSN 1290-0729

Any correspondence concerning this service should be sent
to the repository administrator: tech-oatao@listes-diff.inp-toulouse.fr

Turbulent flow and transient convection in a semi-annular duct

N. Baudin ^{a, b, *}, C. Colin ^b, P. Ruyer ^a, J. Sebilliau ^b

^a Institut de Radioprotection et de Sûreté Nucléaire (IRSN), PSN-RES/SEMIA/LIMAR, BP3, St Paul-Lez-Durance, 13115, France

^b Institut de Mécanique des Fluides de Toulouse, Université de Toulouse, CNRS, Allée Camille Soula, Toulouse, 31400, France

Keywords:

Semi-annulus

Turbulent flow

Transient convection

Turbulent flow and heat transfer in an annular geometry have been previously studied experimentally or numerically. Velocity and temperature profiles have been measured and correlations for the wall shear stress and heat transfer have been derived. However there exists no study in turbulent flow for a semi annular geometry. This work aims to study steady and transient convection in a semi annular test section for a wide range of Reynolds numbers from 10,000 to 60,000, the inner cylinder being heated by Joule effect. The velocity profile in the symmetry plane is measured by Particle Image Velocimetry and the temperature of the inner heated cylinder is measured by infrared thermography. The experimental results are complemented by numerical simulations which give also access to the velocity and temperature profiles in the whole test section.

These results are compared to those obtained in an annular geometry for the same inner and outer cylinders radii and an equivalent flow rate. The velocity and temperature profiles and the wall shear stress are the same as in an annular section in an angular sector of $\pi/2$ around the symmetry plane. Both velocity and temperature profiles follow a logarithmic law. In steady convection, the local heat transfer has been characterized in several azimuthal positions. The local Nusselt number can be expressed versus a Reynolds number based on the local friction velocity. Characteristic thermal boundary layer thicknesses are also defined. Finally, transient convection tests are performed with a square power generation. The wall heat transfer and the evolution of the liquid temperature near the wall have the same self similar evolution, with a characteristic time scale, which only depends on the flow Reynolds number.

1. Introduction

The core of a Pressurised Water Reactor (PWR) contains thousands of cylindrical fuel rods. Between them, some control rods allow controlling the nuclear reaction. All these rods are immersed in high pressure water that acts as coolant and moderator fluid. If a control rod is accidentally ejected, a local and sudden reactivity increase happens leading to a reactivity initiated accident (RIA). It leads to an increase of the rod temperature with first convective heat transfer and then boiling heat transfer. There is still a lack of knowledge for the rod's clad to coolant heat transfer in those transient conditions. The present study takes part of the research program defined by IRSN (Institut de Radioprotection et de Sûreté Nucléaire) on this topic.

For a RIA, the wall to fluid heat transfer till the onset of nucleate

boiling occurs over a very short time scale. Therefore, only the very near wall flow and heat transfer has a relevant impact on the fuel rod behavior. The transient is thus studied only around a single rod surrounded by a vertical flow. The latter is idealized as a flow in an annular cross section with equivalent hydraulic diameter of the typical sub channel defined between neighboring rods (in yellow in Fig. 1). To conduct experiments in a simple geometry but similar to this sub channel, an experimental set up was designed by Visentini et al. [1]. To measure the wall temperature with a high temporal and spatial precision, the infrared thermography is used and so an optical access to the wall is needed. Therefore a half annular cross section with the heated inner half cylinder has been preferred to the annular one. Before the boiling incipience, heat is transferred from the wall to the liquid by single phase convection. It is thus necessary to characterize the velocity and temperature fields and heat transfer in a semi annular geometry. Depending on the power generation in the heated wall, the convection is either steady or transient.

In the literature, the studies concerning heat transfer in annular

* Corresponding author. Institut de Mécanique des Fluides de Toulouse, Université de Toulouse, CNRS, Allée Camille Soula, Toulouse, 31400, France.

E-mail address: baudin.na@gmail.com (N. Baudin).

Nomenclature

Greek symbols

α	Thermal diffusivity, $\alpha = \frac{\lambda}{\rho C_p}$, ($\text{m}^2 \text{s}^{-1}$)
β	Isobar expansion coefficient (K^{-1})
δ	Boundary layer thickness, (m)
γ	Apex angle of the cross section
κ	Von Karman constant
λ	Thermal conductivity, ($\text{W m}^{-1} \text{K}^{-1}$)
μ	Dynamic viscosity, (Pa s)
ν	Cinematic viscosity, ($\text{m}^2 \text{s}^{-1}$)
ϕ	Heat flux, (W m^{-2})
Φ_h	Enthalpy flux, (W m^{-1})
ρ	Density, (kg m^{-3})
τ	Total shear stress, ($\text{m}^2 \text{s}^{-2}$)
θ	Azimuthal angle

Latin symbols

\mathcal{I}	Current (I)
\mathcal{P}	Generated power, $\mathcal{P} = \mathcal{U}\mathcal{I}$, (W)
\mathcal{U}	Voltage (V)
$\frac{dp}{dz}$	Pressure gradient, (Pa m^{-1})
A, A'	Constants
Bi	Biot number, $Bi = \frac{h e_w}{\lambda_w}$
C_p	Specific heat capacity, ($\text{J kg}^{-1} \text{K}^{-1}$)
D_h	Hydraulic diameter (m)
e_w	metal foil thickness, (m)
f_D	Darcy friction coefficient, $f_D = \frac{dp}{dz} \frac{D_h}{0.5 \rho u_m^2}$
f_F	Fanning friction factor, $f_F = \frac{\tau_{w,m}}{0.5 \rho u_m^2}$
g	Gravity acceleration, (m s^{-2})
Gr	Grashof number, $Gr = \frac{g \beta \Delta T D_h^3}{\nu^2}$
h	Heat transfer coefficient, $h = \frac{\phi_w - T_f}{T_w - T_f}$, ($\text{W m}^{-2} \text{K}^{-1}$)
k_e	Turbulent kinetic energy, $k_e = 0.5(u'^2 + v'^2 + w'^2)$, ($\text{m}^2 \text{s}^{-2}$)
Nu	Nusselt number, $Nu = \frac{\phi_w D_h}{\lambda (T_w - T_b)}$
Pr	Prandtl number, $Pr = \frac{\nu}{\alpha}$
Q	Flowrate ($\text{m}^3 \text{s}^{-1}$)

r	Radial position (m)
r^*	Dimensionless radial position, $r^* = \frac{r - r_i}{r_o - r_i}$
r_0	Radial position of the zero of total shear stress (m)
Re	Reynolds number, $Re = \frac{\rho u_m D_h}{\mu}$
S	Surface section (m^2)
T	Temperature, (K)
t	Time, (s)
T^*	Dimensionless temperature, $T^* = \frac{T_w - T_b}{T_w - T_i}$
T^+	Dimensionless temperature, $T^+ = \frac{T_w - T_i}{T_f - T_i}$
t_c	Characteristic time to establish stationary convection, (s)
T_f	Friction temperature, $T_f = \frac{\phi_w}{\rho C_p u_m}$, (K)
u	Axial velocity, (m s^{-1})
u', v', w'	Turbulent velocities, (m s^{-1})
u^*	Friction velocity $u^* = \sqrt{\frac{\tau_w}{\rho}}$, (m s^{-1})
u^+	Dimensionless axial velocity, $u^+ = \frac{u}{u^*}$
u_m	Mean velocity $u_m = Q/S$, (m s^{-1})
y	Radial position from the inner wall, $y = r - r_i$ (m)
y^+	Dimensionless position, $y^+ = \frac{\rho y u^*}{\mu}$

Subscripts

θ	At a given azimuthal position
b	Bulk
eq	Equivalence between annular and semi annular geometries
exp	Experimental
gen	Generated by Joule effect
i	Inner wall
$inlet$	Inlet
l	Liquid
m	Mean
max	Maximum
o	Outer wall
$simul$	Simulated
$stat$	Stationary
th	Theoretical
w	Wall

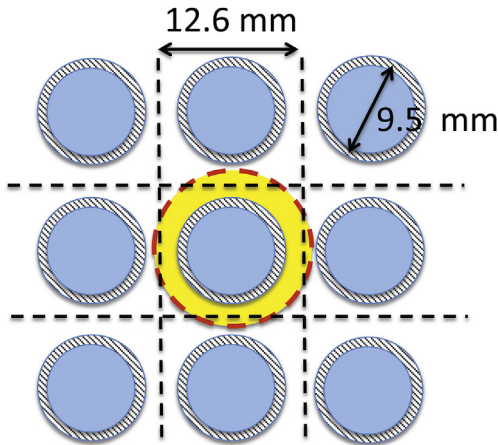


Fig. 1. Scheme of fuel rods and sub-channel.

sector ducts mainly concern heat exchangers. The cross section (Fig. 2) is characterized by the inner and outer wall radii r_i and r_o and the apex angle γ . Sparrow et al. [2], Soliman et al. [3] and Ben Ali et al. [4] studied heat transfers in sector annulus with apex

angles from 5° to 350° . However, these studies are all in laminar flow. Several studies were also performed in turbulent flows with different inner and outer radii, apex angle, Reynolds number Re , fluids, heated walls (Table 1). Tao et al. [5] and Li et al. [6] studied turbulent flow and heat transfer in sector annulus with apex angles from 18° to 40° . The boundary conditions for the heat transfer are different from ours because they heat the outer wall. Li et al. found that the friction factor increases with the apex angle and varies from 0.03 to 0.02 when the Reynolds number Re ranges from 10,000 to 50,000 for a 40° apex angle.

Another geometry of interest is the annular geometry, for which there are a lot of studies. Kang et al. [7] conducted experiments for isothermal and heated turbulent upward flow in a vertical annular channel. The inner part is heated with a steady heat flux and the fluid is a refrigerant R 113. They measured liquid velocity profiles with laser Doppler velocimetry and the temperature field with a cold wire. Using the same test section, Hasan et al. [8] deduced a correlation for the Nusselt number Nu versus the Reynolds number Re and the Prandtl number Pr :

$$Nu = 0.0106 Re^{0.88} Pr^{0.4} \quad (1)$$

It is known that the correlations in convection depend on the

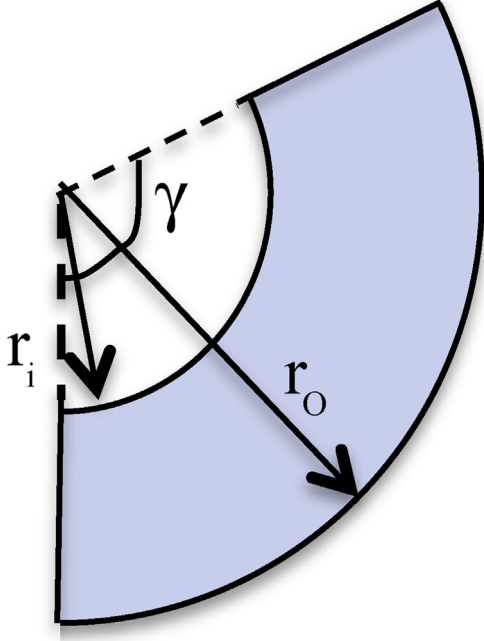


Fig. 2. Scheme of annular sector cross section.

working liquid: water, liquid metal or refrigerant. Since we also use a refrigerant in our experiments and a similar heating of the inner cylinder, eq. (1) will be used for comparison with our results.

Kaneda et al. [10] developed a model for a turbulent flow and convection in an annulus, validated by many numerical results and the experimental results of Rehme [9]. The mean velocity u_m is defined with the flowrate Q by $u_m = Q/S$, S being the surface of the cross section of the duct. The Reynolds number of the duct writes $Re = \frac{\rho u_m D_h}{\mu}$ where ρ is the fluid density, μ the dynamic viscosity and D_h the hydraulic diameter. The local velocity and distance to the wall y are scaled by the friction velocity u^* :

$$u^+ = \frac{u}{u^*} = u \sqrt{\frac{\rho}{\tau_w}} \quad (2)$$

$$y^+ = \frac{\rho y u^*}{\mu} = \frac{\rho(r - r_i) u^*}{\mu} \quad (3)$$

r being the radial position. The wall shear stresses τ_w can be calculated from the mean Fanning friction factor f_F (Kaneda et al. [10]):

$$f_F = \frac{\tau_{w,m}}{\frac{1}{2} \rho u_m^2} \quad (4)$$

$$\tau_{w,m} = \frac{r_i \tau_{w,i} + r_o \tau_{w,o}}{r_i + r_o} \quad (5)$$

$$\frac{\tau_{w,i}}{\tau_{w,o}} = \frac{r_o}{r_i} \left(\frac{r_o^2}{r_i^2} \frac{r_i^2}{r_o^2} \right) \quad (6)$$

r_0 being the position where the total shear stress is equal to zero. It is calculated according to Rehme [9]:

$$\frac{r_0}{r_o} = \frac{r_i}{r_o} \left(\frac{r_i}{r_o} \right)^{0.386} \quad (7)$$

For the Fanning friction factor, Kaneda et al. propose the following equation:

$$\sqrt{\frac{2}{f_F}} = 1.61 + \frac{1}{0.436} \ln(Re) - \frac{550}{Re \sqrt{f_F}} - \frac{1}{0.436} \ln\left(\sqrt{\frac{2}{f_F}}\right) \quad (8)$$

With eq. (8), we calculated that the friction factor in an annular duct is much lower than the one in a sector annular duct, where there is a strong influence of the side walls. For the dimensionless velocity, Kaneda et al. [10] propose the following log law:

$$u^+ = A + \frac{1}{\kappa} \ln(y^+) \quad (9)$$

where they suggest to take $A = 6.13$ and to set the Von Karman constant $\kappa = 0.436$.

To our knowledge, there is no study of turbulent convection in a semi annulus while the annular geometry is well documented. The objective of this work is to characterize flow velocity and heat transfer in a semi annular geometry and to derive scaling laws for the wall friction and heat transfer in different azimuthal positions for a wide range of Reynolds numbers. The velocity field in the symmetry plane is measured by PIV for a wide range of Reynolds number Re . The temperature of the heated wall is measured by Infrared Thermography in the symmetry plane. 3D numerical simulations with the software STAR CCM+ are also performed and allow to quantify the velocity and temperature profiles in the whole cross section. They also give access to the wall shear stress and wall temperature at all azimuthal positions.

Firstly in Section 2, we describe the experimental set up and the measurement techniques: PIV measurements and infrared thermography. Because of technical constraints, we can only measure quantities in the symmetry plane of the semi annulus section. To investigate the whole section, we performed numerical simulations with the software STARCCM+. Thus in Section 3, we present the computation method used and the validation of the mesh by comparison with results of the literature.

In Section 4, the characteristics of the turbulent flow in the semi annulus are presented: mean velocity profiles, turbulent kinetic energy and turbulent shear stress profiles, friction velocity. They are compared to results obtained in an annular cross section

Table 1
Studies of flow and heat transfer in sector-annulus.

Authors	Fluids	$\gamma(^{\circ})$	$r_i(\text{mm})$	r_i/r_o	$10^3 Re$	$\phi_w (\text{kW m}^{-2})$
Tao et al. [5]	Air	18-40	9-16	0.25	5-50	Outer wall
Li et al. [6]	Air	18-40		0.2-0.5	10-50	Outer wall
Kang et al. [7]	R113	360	7.9	0.415	22-46.4	0, 9, 16 (in. wall)
Hasan et al. [8]	R113	360	7.9	0.415	22-46.4	0, 9, 16 (in. wall)
Rehme [9]	Air	360	2-10	0.02-0.1	20-200	
Kaneda et al. [10]	Air	360		0.001-0.999	20-200	

and to correlations of the literature. The flow is also characterized at different azimuthal positions. In Section 5, the steady convection is studied. The temperature profiles in the liquid are determined and characteristic thermal boundary layer thicknesses are defined. The heat transfer coefficient is evaluated and compared to the one obtained in annular flow. Then a local heat transfer coefficient depending on the azimuthal position is also determined. Finally the transient convection is studied and a similarity law for the evolution of the wall temperature and the development of the thermal boundary layer thickness is proposed.

2. Experimental set-up and measurements techniques

In this section, we introduce the main features of the facility. More details can be found in [1]. The test section has a semi annular section. The inner half cylinder consists of a 50 μm thick stainless foil heated by Joule effect. Its diameter is 8.4 mm and its length 200 mm. The outer part consists of a 34 mm internal diameter glass half cylinder (Fig. 3). The semi annular section is filled with a coolant 1 methoxyheptafluoropropane ($\text{C}_3\text{F}_7\text{OCH}_3$), which will be referred as HFE7000 (3 M). This fluid has been chosen because of its low saturation temperature (35 $^\circ\text{C}$ at atmospheric pressure), its low latent heat of vaporisation (ten times smaller than the water one), and the smaller critical heat flux value compared to water. These characteristics have been chosen to perform highly transient boiling experiments with a lower power than required for water. The main physical properties of HFE7000 at saturation temperature and atmospheric pressure are given in Table 2, where ρ , C_p , λ and ν are the density, heat capacity, thermal conductivity and kinematic viscosity, respectively.

The metal half cylinder is glued to two lateral quartz glass plates (thickness: 3 mm, width: 42 mm, length: 200 mm). The plates, together with the foil, are placed in an aluminum cell. In this cell, a visualization box filled with HFE7000 is used to reduce optical distortions (Fig. 3). The experiments are carried out in flow boiling conditions by inserting the test cell in a two phase flow loop consisting of a gear pump, a Coriolis flow meter, a preheater, a 1 m long channel upstream the test section to establish the flow and a condenser.

The electrical power is provided by a power supply SORENSEN SGA. It covers the 0–40 V voltage range and the 0–250 A current range. The power supply is driven by an arbitrary generator where all kind of signals can be programmed. The power supply can provide a current increase up to 45 A s^{-1} . A voltmeter and an ammeter measure the tension \mathcal{U} and current \mathcal{I} to calculate the generated power in the metal foil $\mathcal{P} = \mathcal{U}\mathcal{I}$.

Particle Image Velocimetry measurements are carried out in the

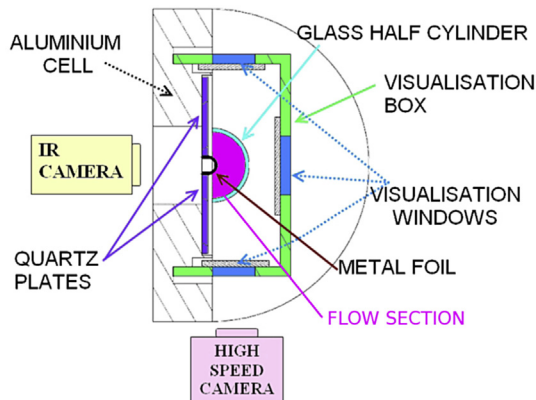


Fig. 3. Schema of the test section, Visentini et al. [1].

Table 2
HFE7000 properties at saturation temperature and at atmospheric pressure.

ρ (kg m^{-3})	C_p ($\text{J kg}^{-1} \text{K}^{-1}$)	λ ($\text{W m}^{-1} \text{K}^{-1}$)	ν ($\text{m}^2 \text{s}^{-1}$)
1385.8	1300	0.075	$3.2 \cdot 10^{-7}$

symmetry plane of the test section (Fig. 4). The laser used is a "Nd:YAG" QUANTEL TWIN ULTRA with a wavelength of 532 nm and an energy of 30 mJ for two pulses of 7 ns at 15 Hz. The time interval between the 2 pulses of the laser is varied between 80 and 140 micro seconds depending on the flow velocity. Images are recorded by a Sencicam PCO camera with an optical MACRO NIKON lens of 105 mm. The resolution of the CCD sensor is $1376 \times 1040 \text{ px}^2$. Methyl Metacrylate spheres with encapsulated Rhodamine B are used for seeding the flow. They have a mean diameter of 10 μm . The Stokes number associated to these particles in the flow has been evaluated. It is equal to the ratio of the response time of the seeding particles of density ρ_p : $t_p = \rho_p \cdot d_p^2 / \mu = 0.1 \text{ ms}$ over the response time of the flow $t_f = le/u^*$ 0.3 s, where le is the integral length scale. The Stokes number is below 0.05 for our experiments.

The mean velocities and RMS values are calculated with the software Davis. They are calculated with cross correlations in three passes, first on $64 \times 64 \text{ px}^2$ windows to finish with $16 \times 16 \text{ px}^2$ windows, with an overlap of 50%. The convergence of mean and RMS values of the velocity is reached with about 1000 images. The optical distortions are negligible near the inner cylinder but are important near the outer one. The experimental velocity distribution is thus not studied in this area.

The metal foil is painted in black in order to increase its emissivity (the emissivity of the paint is 0.94). Thermal measurements are performed with an infra red camera looking at the foil from backward (see Fig. 3). A CEDIP JADE III camera with a sensitivity range between 3.5 and 5.1 μm is used. It has a focal plane array type and a Stirling cooled MCT detector of $240 \times 320 \text{ px}^2$. For this study, the acquisition frequency is 150 fps and the height of the metal foil investigated is about 7 cm. The infra red camera is calibrated thanks to a DCN 1000 N4 black body. The uncertainty on the measurement temperature is about $\pm 0.6 \text{ }^\circ\text{C}$ at 20 $^\circ\text{C}$ and $\pm 0.2 \text{ }^\circ\text{C}$ at 70 $^\circ\text{C}$. It takes into account the non uniformity of the black body temperature surface and the noise on the camera sensor.

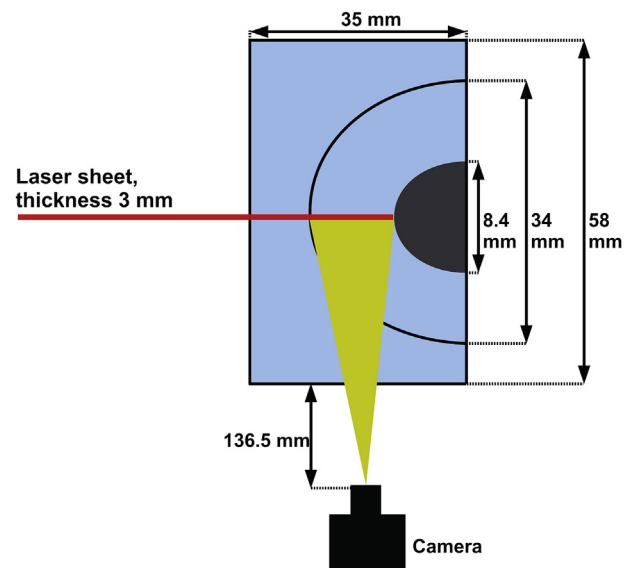


Fig. 4. Schema of PIV measurements.

Due to the very low heat transfers between air and the back of the foil, this surface is assumed adiabatic. The thermal gradient across the foil thickness is expected to be negligible, since the Biot number Bi characterizing the thermal resistance of the foil by comparison to the thermal resistance of the flow is very small. For a high heat transfer coefficient characteristic of convection $h = 1000 \text{ W m}^{-2} \text{ K}^{-1}$, the Biot number is equal to $Bi = h \cdot e_w / \lambda_w = 0.003$, e_w being the foil thickness and λ_w its thermal conductivity. Due to the small value of Bi , in the following the wall temperature measured by the infra red camera at the backside of the metal foil will be considered equal to the temperature of the wall in contact with the fluid. Moreover, the diffusion time across the foil thickness, $e_w^2 / \alpha_w = 0.6 \text{ ms}$, is actually small enough to assume that there is no time lag between the thermal evolution of both sides of the metal foil. e_w is the metal foil thickness and $\alpha_w = 4.08 \cdot 10^{-6} \text{ m}^2 \text{ s}^{-1}$ its thermal diffusivity. Thus, it is possible to measure the temperature of the wall that is in contact with air, in order to know the temperature of the wall that is wetted by the refrigerant.

The heat flux transmitted to the liquid is calculated from the power generated in the metal foil by Joule effect ϕ_{gen} and from the energy stored in the foil itself. A calculation of the 2D transient heat conduction in the metal foil and the quartz plates has been performed using COMSOL Multiphysics and showed that there are limited losses toward the quartz planes (Visentini [11]). It is possible to estimate the heat flux ϕ_w transferred to the fluid by a simple thermal balance:

$$\phi_w = \phi_{gen} - \rho_w \cdot C_{pw} \cdot \frac{dT_w}{dt} \cdot e_w \quad (10)$$

where $\rho_w = 7930 \text{ kg m}^{-3}$, $C_{pw} = 500 \text{ J kg}^{-1} \text{ K}^{-1}$ and $\frac{dT_w}{dt}$ are the density, the heat capacity of the foil and the wall variation of temperature, respectively. In this article, the temperature and the heat flux measurements are averaged on a 1 cm height by 2 mm width area.

A National Instruments box is used to acquire the thermocouples signals. Three K type thermocouples measure the HFE7000, air, and infrared camera temperatures.

The uncertainties of the electronic devices (ammeter, National Instrument box) are very low and of the order of magnitude of 0.1% (Visentini [11]). The power generated by Joule effect per surface unit ϕ_{gen} is equal to $\mathcal{U} \cdot \mathcal{I} / L \cdot l$ where L the length of the foil and l its width. The main uncertainty is on the length of the part where the voltage is measured (about $\pm 0.2 \text{ cm}$ on 8.5 cm i.e. about 2%). Thus the total uncertainty on ϕ_{gen} is 2.5%. The heat transfer from the wall to the fluid is calculated with eq. (10). Assuming that $\rho_w C_{pw} e_w = 198.3 \text{ J m}^{-2}$ has no uncertainty, the absolute uncertainty on the heat flux is:

$$\frac{\Delta \phi_w}{\phi_w} = \frac{\Delta \phi_{gen}}{\phi_{gen}} \cdot \frac{\phi_{gen}}{\phi_w} + \frac{\rho_w C_{pw} e_w \Delta(dT/dt)}{\phi_w} \quad (11)$$

The ratio ϕ_{gen} / ϕ_w never exceeds 2 in the experiments. In steady state, the uncertainty on the heat flux is below 5%. In transient convection, the heat flux is generally above 10 kW m^{-2} and the uncertainty on dT/dt is less than 2 K s^{-1} , so, the absolute uncertainty on the heat flux is below 10%.

3. Numerical simulations: details and validation

Simulations are conducted with the software STAR CCM + to investigate the velocity and temperature fields in the whole test section. First the numerical model and the mesh grid are presented. The validation results are provided in the corresponding result

sections of the present paper. The numerical simulations are first validated in a 2D axisymmetrical configuration by comparison with experimental and theoretical results in annular flow. Finally 3D numerical simulations in a semi annular geometry are performed in adiabatic conditions, in steady and transient convection.

The flow is modeled in two regions. The turbulent flow is computed by using a $k-\epsilon$ model far from the walls and a low Reynolds model near the walls. The space scheme used is a hybrid Gauss LSQ gradient method. The simulations of transients are computed with a 2nd order implicit scheme in time, with a time step of 1 ms. To reproduce the experiment, the metal foil is modeled and the Joule power generation is simulated by a volumetric heat source. The time step was validated by transient simulations of conduction with comparison with the analytical result from Carslaw and Jaeger [12]. The numerical simulations are performed with a wall heated by Joule effect corresponding to heat flux of $20,000 \text{ W m}^{-2}$ on one side and an adiabatic wall at a distance of 13 mm.

A polyhedral mesh is used in the cross section with cells size about 0.1 mm in the center region. This mesh is plotted in Fig. 5 for the semi annular geometry. Due to symmetry consideration, only one half of the cross section is meshed. Face a is a symmetry axis, faces b , c and d are wall boundary conditions. Close to the walls (b , c and d) for $y^+ < 60$ a refined mesh consists of n cells with a stretching of 1.1 (according to the user guide), n being between 20 and 60 (Fig. 6). For 2D axisymmetrical simulations a slide of the computation domain between two symmetry planes is used. The refined mesh in the two wall regions is also used. This mesh has been validated by comparison of numerical simulations with experimental results of Kang et al. [7]. In the flow direction, the cross sectional mesh is extruded into 100 layers on 1 m. This length has also been extended to 2 m depending on the establishment length of the flow. A convergence study has been performed. For a cell size of 0.1 mm in the center region, the results are sensitive to the number n of cells in the near wall region. For $n > 20$, the results are converged.

Concerning the flow computation, the mass, momentum, energy balance equations can be solved in decoupled or coupled manner. The complete formulation can be described as using a collocated variable arrangement (as opposed to staggered) and a Rhie and Chow type pressure–velocity coupling combined with a SIMPLE type algorithm. $k-\epsilon$ turbulence model is used in the most part of the flow except close to the wall ($y^+ < 60$) where a low Reynolds model is used. The time step is taken equal to 0.001 s with

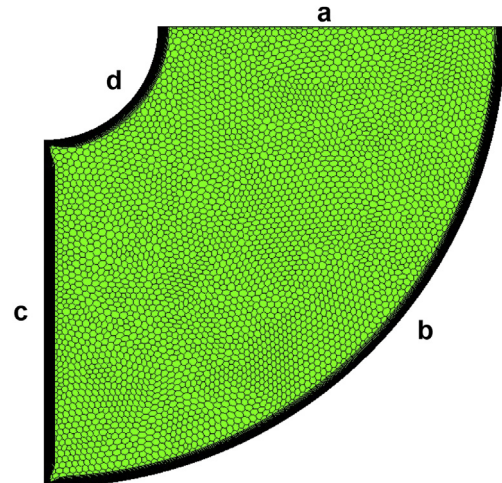


Fig. 5. Mesh of the cross section.

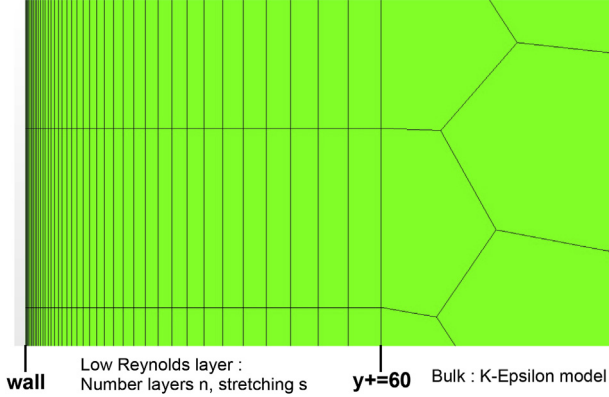


Fig. 6. Refined mesh close to the wall.

10 iterations per time step. The convergence criteria is a critical value of the residus smaller that 0.01 on mass, energy and dissipation rate of the TKE and 0.001 on the other variables. Computation are performed on a PC with 8 cores Xeon(R) E5 1650 0 @ 3.20 GHz. The computation time ranges between a few hours (for 2D axisymmetrical simulations) to a few days (3D simulations).

Numerical simulations are first validated by comparison with the experimental results of Kang et al. [7] with R113 in an annular geometry with inner and outer radii $r_i = 7.9$ mm and $r_o = 19$ mm. Fig. 7 shows a comparison of the velocity profiles for experiment 4 with a Reynolds number of $Re = 31,500$ and two adiabatic walls. The mesh previously described is used for the simulations. There is a good agreement between the simulation, the experiment and the log law proposed by Kaneda (eq. (9) with u^* calculated from eqs. (6)–(8)). In the central region ($0.003 < r - r_i < 0.007$), we observe a slight difference between the model and both the experimental and simulated data. In the theory, this region is simply the junction of two wall laws that could explain this difference. In the near wall region, we can observe a slight difference between experimental results and both theory and simulations. The origin of this difference may reside in the difficulty to make accurate measurements near the wall.

For the convection simulations, the turbulent Prandtl number is set to 0.9 as deduced from Kang et al. [7] with experimental data in an annulus. To estimate the importance of thermal convection compared to the forced convection, we calculate the Richardson number, which is ratio of the Grashof number $Gr = \frac{g\beta\Delta T D_h^3}{\nu^2}$ over the Reynolds number squared. g is the gravity acceleration, β the isobar expansion coefficient and ΔT a characteristic difference

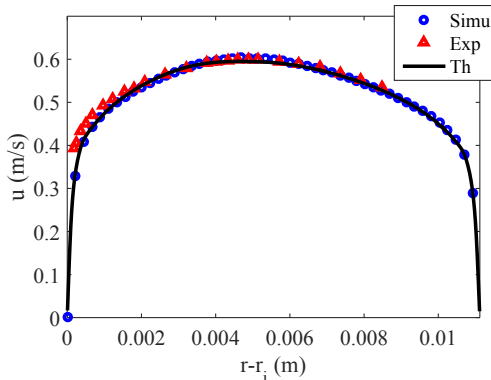


Fig. 7. Velocity profile for an annulus filled by R113 without heating ($r_i = 7.9$ mm, $r_o = 19$ mm, $Re = 31,500$), experiment 4 from Kang et al. [7].

temperature between the wall and the liquid. In the experiments, the ratio Gr/Re^2 is between 0.001 and 0.1. Thus there is no significant buoyancy effect. Simulations with Boussinesq's approximation also show that buoyancy effect is negligible.

The outlet fields calculated in adiabatic flow simulations are used as inlet and initial conditions for the simulations with wall heat transfer. In these calculations, only the 20 cm heated length is simulated, and is discretized in 500 layers in the axial direction. The wall to fluid heat flux is set to $\phi_w = 20,000$ W m⁻² and the inlet temperature is set to 300 K. These values are averages from the experimental values.

To validate the convective simulations, we use again the results from Kang et al., in particular the experiment 5. The wall to fluid heat flux $\phi_w = 9000$ W m⁻² is the boundary condition and the Reynolds number is $Re = 22,800$. The inlet temperature is equal to 316 K and the initial temperature of the fluid and the wall is also equal 316 K. Fig. 8 shows temperature profiles from experiment 5 in Kang et al. [7] and simulation. As for velocity fields, the agreement between the numerical simulations and the experimental results is good. Additional numerical simulations were also performed in a 3D geometry with a mesh similar to Fig. 5, between 2 symmetry planes a and c . The results are in very good agreement with those of the 2D axisymmetrical simulations. The mesh is well adapted to the computation for both velocity and temperature fields. The same method of meshing is adopted to simulate the semi annular flow.

4. Turbulent flow in a semi-annulus

To analyse the wall to fluid heat transfer, the study of the velocity distribution is needed. Experimental and numerical results in the symmetry plane are first compared. Then we study the shear stress and velocity field in the whole cross section.

We want to compare our results in a semi annular geometry with the results in the annular geometry from Kaneda et al.'s theoretical. To have an equivalence, we choose to keep the same inner and outer radii r_i and r_o and so, to vary the flowrate Q . The equivalent flowrate Q_{eq} for the annular geometry is calculated to have the same maximum velocity u_{max} as in the symmetry plane of the semi annular geometry. The parameters corresponding to different experimental runs are gathered in Table 3. The value of the ratio $\frac{Q_{eq}}{Q}$ is constant (around 2.2) for Reynolds number values larger than 15,000. Simulations of the flow were computed with HFE7000 properties and it seems that the ratio $\frac{Q_{eq}}{Q}$ is independent from the fluid used. It may be only a geometry characteristics which can be explained as follows: the annulus area is twice the semi annulus

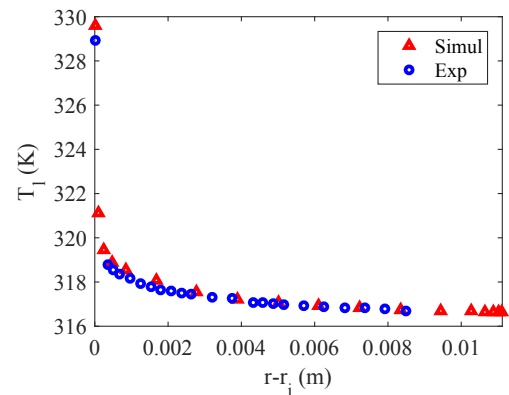


Fig. 8. Temperature profile for an annulus filled by R113 with the inner cylinder heated ($r_i = 7.9$ mm, $r_o = 19$ mm, $Re = 22,800$, $\phi_w = 9000$ W m⁻², $T_{inlet} = 316$ K), experiment 5 from Kang et al. [7].

area so, to have the same maximum of velocity, the flow rate must be at least twice too. Moreover, out of the symmetry plane in the semi annular geometry, and due to the friction against the lateral walls, the velocity magnitude is always less than the maximum in the symmetry plane. Since in an annular geometry the velocity profile is the same everywhere, the equivalent flow rate must be larger than the semi annular flow rate. The ratio $\frac{Q_{eq}}{Q}$ is not far from 2 so we can guess that a great part of the semi annulus has a velocity profile very similar to the symmetry plane profile.

The mean axial velocity u and the axial and radial fluctuating velocities u' and v' are measured in the symmetry plane of the semi annular geometry by PIV for different Reynolds numbers, as previously described. The numerical simulations are performed by STAR CCM + using the mesh displayed in Figs. 5 and 6. In the streamwise direction the computation domain is 1.4 m long with a mesh length of 1 cm.

Fig. 9 shows the axial velocity profiles for the Reynolds numbers 8700, 17,400 and 26,500. The experimental, theoretical (eq. (9)) and simulated profiles are similar, with absolute errors less than 5%. There is the same asymmetry of the profiles in annular and semi annular geometries with a shift of the radial position of the maximum axial velocity toward the inner wall. There is only a slight difference because the semi annulus profile is a little less shifted. The profiles of the simulated and theoretical total shear stress (Fig. 10) are similar too. The inner and outer wall shear stresses in the equivalent annular geometry well model the ones in semi annular geometry. The location of the zero in the total shear stress is also shifted toward the inner wall with the same difference between annular and semi annular geometry. The difference between the inner and the outer wall shear stresses explains the asymmetry of the velocity and total shear stress profiles.

Fig. 11 shows experimental and simulated profiles of turbulent kinetic energy $k_e = 0.5\langle u'^2 + v'^2 + w'^2 \rangle$, with u' , v' and w' the axial, radial and azimuthal turbulent velocities, and $\langle \rangle$ is the symbol for time average. We did not measure the azimuthal component of the turbulent velocity so, to calculate k_e we assume orthotropy between radial and azimuthal velocity fluctuation and therefore $w' = v'$.

The wall shear stress can be deduced from the velocity profiles. Due to a slight uncertainty on the inner wall position, a log law is assumed with the same parameters as in Kaneda et al. [10] (eq. (9)) and then an optimization to have the log law in a range of y^+ between 30 and 100 is conducted. The values obtained are given in Table 4. The theoretical friction velocities at the inner wall u_{i0}^* and outer wall u_{o0}^* are calculated with eq. (6). The experimental, theoretical and simulated data are in good agreement. The simulated wall shear stress is given by the software STAR CCM+ and not calculated with the theoretical parameters: the good agreement is another way to validate the simulations. For the both sides, the equivalent annular flow has the same shear stress as the semi annular flow. The simulations and theory show that the inner wall shear stress is more important than the outer one. We remind that u^* depends on the fluid characteristics and the Reynolds number, instead of the ratio u^*/u_m which only depends on the Reynolds number.

Table 3
Flow parameters.

Q (L s ⁻¹)	Re	u_{max} (m s ⁻¹)	Q_{eq} (L s ⁻¹)	Re_{eq}
0.20	8700	0.630	0.44	13,200
0.31	13,400	0.944	0.67	20,200
0.40	17,400	1.238	0.894	26,800
0.51	22,100	1.542	1.122	33,700
0.61	26,500	1.858	1.360	40,800

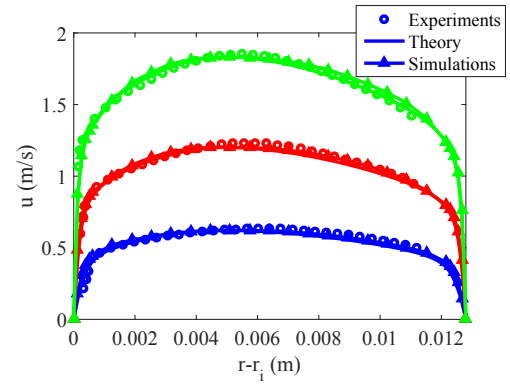


Fig. 9. Mean axial velocity profiles: experiments and simulations in a semi-annulus, theory for an annular geometry - Re 8700 in blue, 17,400 in red and 26,500 in green. (For interpretation of the references to color in this figure legend, the reader is referred to the web version of this article.)

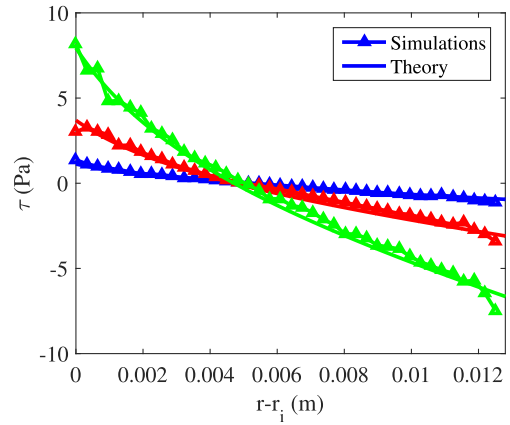


Fig. 10. Total shear stress profiles - Re 8700 in blue, 17,400 in red and 26,500 in green. (For interpretation of the references to color in this figure legend, the reader is referred to the web version of this article.)

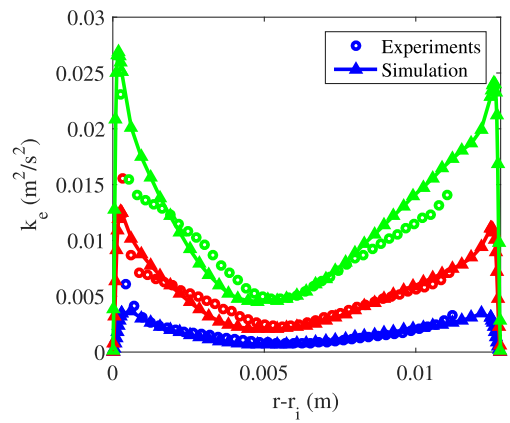


Fig. 11. Turbulent kinetic energy profiles for 3 Reynolds numbers Re 8700 in blue, 17,400 in red and 26,500 in green. (For interpretation of the references to color in this figure legend, the reader is referred to the web version of this article.)

Fig. 12 shows the dimensionless velocity u/u^* . The simulated and experimental profiles are well superimposed with the log law in the y^+ range [30, 300]. The equivalent annular friction velocities are similar to the semi annular ones, for the inner and the outer walls. $u_{i,exp}^*$ is determined by fitting the experimental velocity profile with

Table 4

Friction velocities for all Reynolds numbers.

Re	$u_{i,exp}^*$ (m s ⁻¹)	$u_{i,th}^*$ (m s ⁻¹)	$u_{i,simul}^*$ (m s ⁻¹)	$u_{o,th}^*$ (m s ⁻¹)	$u_{o,simul}^*$ (m s ⁻¹)
8700	0.034	0.034	0.036	0.031	0.032
13,400	0.048	0.049	0.051	0.045	0.046
17,400	0.061	0.062	0.062	0.057	0.056
22,100	0.075	0.076	0.077	0.070	0.070
26,500	0.088	0.090	0.090	0.083	0.081

the log law (eq. (9)) for $A = 6.13$ and $\kappa = 0.436$, as the theory, and so the data are superimposed. It is important to see that the log laws for the simulations are obtained independently, and the agreement with the other curves is also good.

Fig. 13 shows isocontours and radial profiles of the axial velocity at different azimuthal angles θ . We choose the value of the angle θ equal to 0 for the wall (x axis) and $\pi/2$ for the symmetry plane (y axis). The velocity profile does not vary a lot in $\pm\pi/4$ sector around the symmetry plane. For angles larger than $\pi/4$, the profiles tends to symmetrize, i.e. the radial position of the maximum velocity shifts toward the center and the inner and outer wall shear stresses tend to be equal. When the angle tends to 0, i.e. near the walls, the velocity decreases due to the friction. There is the same trend with the inner friction velocity (Fig. 14): the friction velocity does not vary in the quarter near the symmetry plane and decreases near the wall. Since the fluid velocity is higher in the center of the duct, the shear stress is more important in this area.

Integrating the wall shear stress in the cross section, we calculate the pressure gradient along the duct. The Darcy friction factor f_D can be evaluated with:

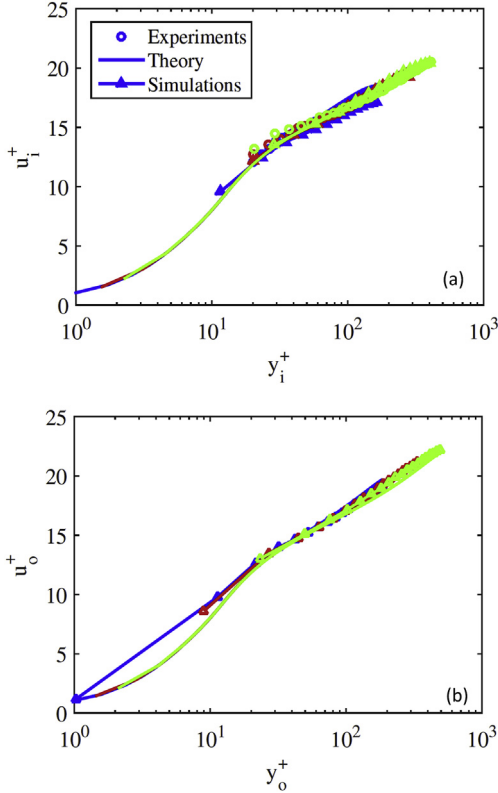


Fig. 12. Comparison of experimental, simulated and theoretical values for $u^+(y^+)$: $Re = 8700$ in blue, 17,400 in red and 26,500 in green (a) inner wall region - (b) outer wall region. (For interpretation of the references to color in this figure legend, the reader is referred to the web version of this article.)

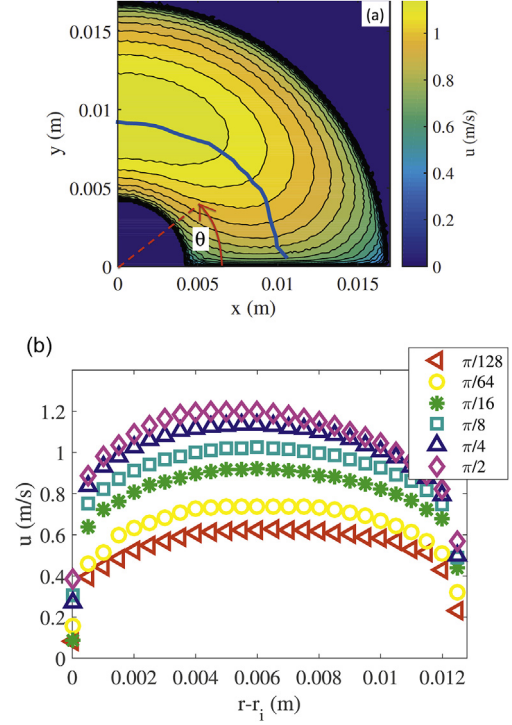


Fig. 13. Axial velocity ($Re = 17,400$). (a) isocontours - (b) velocity profiles at different azimuthal angles.

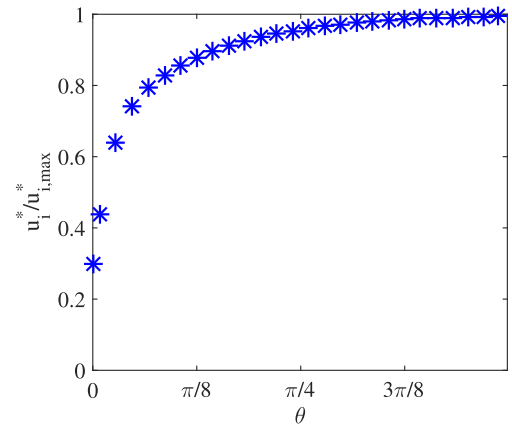


Fig. 14. Normalized friction velocity along the azimuth angle ($Re = 17,400$).

$$f_D = \frac{dp}{dz} \frac{D_h}{0.5\rho u_m^2} \quad (12)$$

The Darcy friction factor f_D is four times the Fanning friction factor f_F and these two definitions are used in function of the

context. On the left hand side of Fig. 15 the friction factors f_D are plotted versus the Reynolds number for different geometries and compared to Blasius correlation for a cylinder $f_D = 0.316Re^{-0.25}$. The friction factor in an annulus and a cylinder are equal, as shown by Kaneda et al. [10]. The friction factor is also similar between the semi annular and annular sector geometries. However, there is a difference between the sector annular geometries ($\gamma = 40^\circ$) and the annular or cylindrical geometries. The additional walls (in comparison with the cylindrical or the annular geometry), induce a different friction even with the same Re number value based on the flow velocity. Using the equivalent Reynolds number (based on the maximal velocity as defined in Table 3), the different friction factors obtained for the different geometries agree better. These walls slow down the flow, and it is thus relevant to define an equivalence to compare annular and semi annular geometries. That is why we plot the friction factor versus the equivalent Reynolds number Re_{eq} (Table 3) for annular and cylindrical geometries on the right hand side of Fig. 15. In this figure, all curves better superimpose.

As a partial conclusion, the flow in our test section at a given Reynolds number value is similar, in an angular sector of $\pm\pi/4$ around the symmetry plane, to a flow of quasi twice the Reynolds number value in an annular test section of same inner and outer radii. Being an advantage to model this part, it is also a validation of the simplification from the nuclear core geometry. Moreover, the results from the wall shear stress study will help the analysis of the wall heat transfer.

5. Steady convection

In this part we study the steady convection in a semi annulus with an imposed heat flux at the inner wall in a test section of 20 cm long, with an imposed heat flux of $20,000 \text{ W m}^{-2}$. This heated section is placed downstream an adiabatic section of 1.4 m long. The flow is steady and established, so we can use the results from the previous part as inlet condition in the heated test section. We study the temperature and heat transfer far from the inlet of the test section, where thermal and dynamic boundary layers are established. It corresponds to a length of about 13 cm from the bottom of the heated part, i.e. $\approx 7D_h$.

We are first interested in the temperature distribution in the symmetry plane of the test section. Fig. 16 shows the radial temperature profiles in the liquid for different values of the Reynolds number. Most part of the liquid is at the bulk temperature T_b and there is an heated boundary layer of only 1 mm thick. The bulk temperature does not vary along the duct and is equal to the fluid inlet temperature.

We define the friction temperature T_f , by analogy with the friction velocity:

$$T_f = \frac{\phi_w}{\rho C_p u_i^*} \quad (13)$$

The temperature difference between the wall and the liquid scaled by this friction temperature is plotted in Fig. 17 versus y^+ and follows a log law (eq. (15)).

$$T^+ = \frac{T_w - T_l}{T_f} = \frac{(T_w - T_l)\rho C_p u_i^*}{\phi_w} \quad (14)$$

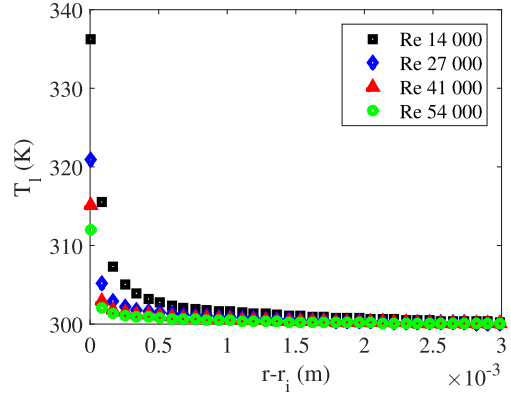


Fig. 16. Liquid temperature profiles.

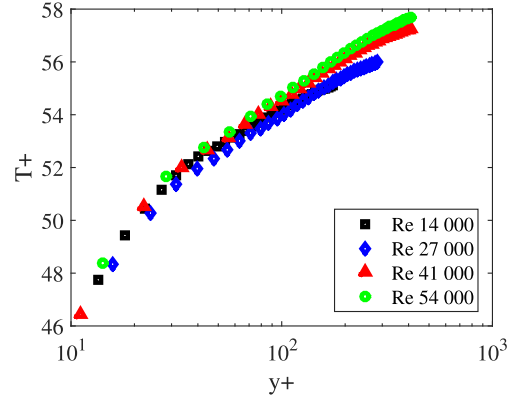


Fig. 17. $T^+(y^+)$.

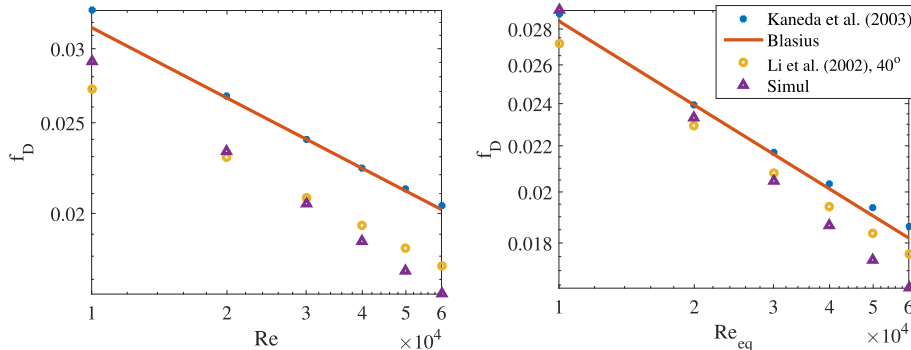


Fig. 15. Darcy friction factor versus the Reynolds number on the left hand side and versus the equivalent Reynolds number on the right hand side.

$$T^+ = A' + \frac{1}{\kappa_T} \ln(y^+) \quad (15)$$

with A' a constant equal to 43.8 and κ_T , the Von Karman constant for the temperature equal to about 0.43.

We found that the ratio of the friction temperature T_f over the temperature difference $T_w - T_b$ is a constant and equal to 0.0176. The Nusselt number Nu is therefore scaled by the friction Reynolds numbers $Re^* = u_i^* D_h / \nu$ as:

$$Nu = \frac{T_f}{T_w - T_b} Pr Re^* = 0.0176 Pr Re^* \quad (16)$$

To study the radial distribution of liquid temperature, we define two different boundary layer thicknesses: the first one is the conventional thermal boundary layer thickness $\delta_{99\%}$ defined as:

$$\frac{T_w - T_l(y = \delta_{99\%})}{T_w - T_b} = 0.99 \quad (17)$$

with T_w and T_l the wall and liquid temperatures respectively. This thickness is scaled by the viscous lengthscale ν/u_i^* and is plotted in the left hand side of Fig. 18. Its evolution can be fitted by the law $\delta_{99\%}^+ = 0.183 Re^{0.7}$ and we see that the values correspond to the upper limit of the log laws validity (for both the velocity and the temperature profiles). It also corresponds to the end of the boundary layer, where the radial heat flux is near zero (for $u_i^* = 0.09 \text{ m s}^{-1}$, $\delta^+ = 150$ corresponds to $\delta = 0.5 \text{ mm}$).

If we consider the bulk temperature as reference, the enthalpy flux Φ_h in the symmetry plane is defined as:

$$\Phi_h = \rho_l C p_l \int_{r_i}^{r_o} u (T_l - T_b) dr \quad (18)$$

We define the second boundary layer δ_h as the thickness of liquid carrying the same enthalpy flux while flowing at the mean velocity $u_{m,\theta=0}$ and being at T_w (the rest of the liquid being supposed at T_b):

$$\Phi_h = \rho_l C p_l (T_w - T_b) u_{m,\theta=0} \delta_h \quad (19)$$

With equations (18) and (19) we calculate δ_h :

$$\delta_h = \int_{r_i}^{r_o} \frac{u}{u_{m,\theta=0}} \left(1 - \frac{T_w - T_l}{T_w - T_b} \right) dr \quad (20)$$

This thickness scaled by the viscous lengthscale ν/u_i^* is plotted in the right hand side of Fig. 18. Its evolution can be fitted by the law

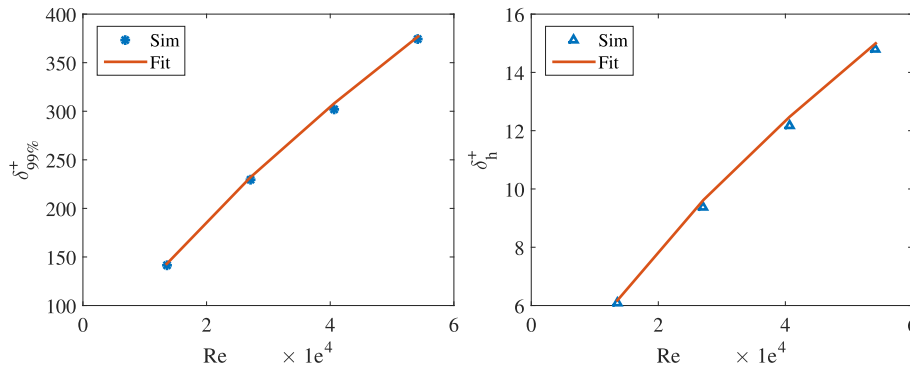


Fig. 18. Thermal boundary layer thicknesses: simulated values and power law fit.

$\delta_h^+ = 0.014 Re^{0.64}$ and we see that the values correspond to the viscous and buffer layers i.e. $\delta^+ < 20$. The thickness δ_h corresponds to the near wall region where the heat flux and the liquid temperature variations are the largest.

The evolution of the Nusselt number with the Reynolds number is plotted in Fig. 19. The experimental and simulated results are similar, and the variation deduced from the log law (eq. (16)) fits the simulation data. We compare these results with two different correlations of the literature: the Dittus Boelter correlation [13] for a cylinder and the Hasan et al. correlation for an annulus. Both of them are calculated with the equivalent Reynolds number. Though these correlations overestimate the Nusselt number, they give a good approximation.

Fig. 20 shows the evolution of the Nusselt number with the azimuthal angle θ . The heat transfer well estimated by eq. (16) where u_i^* is considered as being a function of θ . It fits the experimental data on a large angular sector. The heat transfer is the largest in the mid plane of the cross section where the wall shear stress is the largest, and decreases when θ goes to 0 or π .

The temperature profiles in steady convection can be modeled by two layers. A layer near the heated wall where the radial heat flux is the largest and whose layer is close to the enthalpy layer thickness δ_h (which is about 0.1 mm). The second part corresponds to the log law in the velocity profiles. The radial heat flux is smaller and the thickness of this layer corresponds to the more classical boundary layer thickness $\delta_{99\%}$ which is about 1 mm thick. The temperature in this last part also follows a log law from which we can deduce a relation between the Nusselt number and the wall shear stress. This result is valid for any angle. The simulated results well fit the experimental results and can be also approximated by

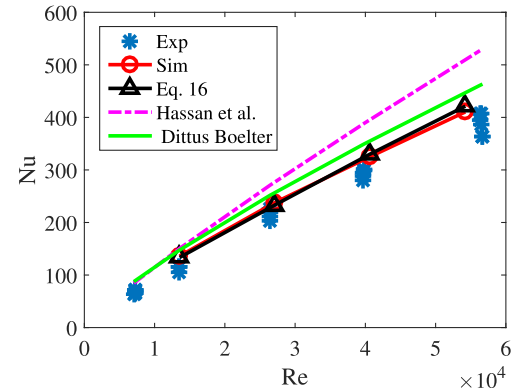


Fig. 19. Comparison between experimental, theoretical and simulated Nusselt numbers versus Reynolds numbers.

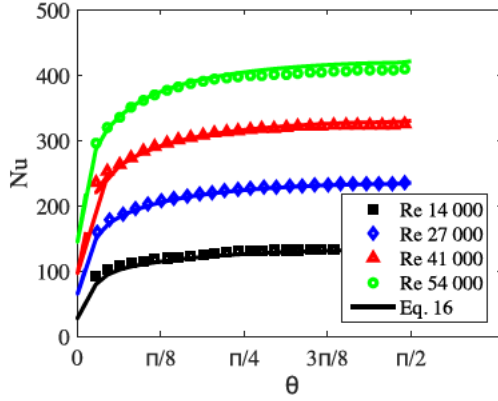


Fig. 20. Evolution of the Nusselt number with the azimuthal location.

Dittus and Boelter or Hasan et al. correlations. In the semi annular cross section the heat transfer coefficient around the symmetry plane (for $\pi/4 < \theta < 3\pi/4$) is the same as in an annular cross section.

6. Transient convection

After studying the steady convection, we are interested in the transient regime toward the steady state. The Joule power generation is set instantaneously to a constant value of 4.10^8 W m^{-3} for a foil thickness of $50 \mu\text{m}$, the wall temperature and heat flux being transient.

We define the difference between the instantaneous wall temperature and the bulk temperature $T_w - T_b$ and we scale it by the difference in steady state $T_{w,stat} - T_b$ to calculate a dimensionless temperature difference $T_w^* = \frac{T_w - T_b}{T_{w,stat} - T_b}$. A characteristic time scale t_c of the transient regime is also defined. To calculate t_c in the experiments, we plot dT_w/dt versus T_w in Fig. 21. The slope of the linear part is equal to $1/t_c$ assuming thus an exponential evolution. In the numerical simulations, the dimensionless profiles all superimpose on a curve described by: $T_w^* = 1 - e^{-t/t_c}$. The experimental profiles differ a little from this idealized trend.

We can calculate t_c on the heating and cooling linear parts with the experimental data in red and black colors, respectively in Fig. 21. The characteristic time scale of the convection t_c is the same in the two transient parts, as in the simulations. It confirms that the calculated value is characteristic of the transient convection.

The characteristic time t_c only depends on the fluid velocity. Fig. 22 shows that t_c decreases when the Reynolds number Re increases. When the fluid velocity increases, the heat transfer is enhanced and the boundary layer becomes thinner, thus the time to reach an equilibrium decreases. We derived an analytical expression to evaluate t_c (details in the appendix):

$$t_c = \frac{\rho_w C_{pw} e_w D_h^2}{\rho C_p D_h \alpha} \frac{1}{Nu_{stat}} \quad (21)$$

This theoretical result fits very well the simulated results, however they are different from the experimental results. We think that this mismatch comes from the difference between the perfect exponential evolution in the simulations and the first instants of the experiments. During this moment, which lasts about 1s for all the tests, the heat transfer differs from the one in the simulations. This difference is probably due to the thermal inertia and heat capacity of the black painting on the back side of the heated foil, which effect may not be negligible for short transients. This effect will be carefully checked in future experiments but can also be taken into account in the numerical simulations by adding the

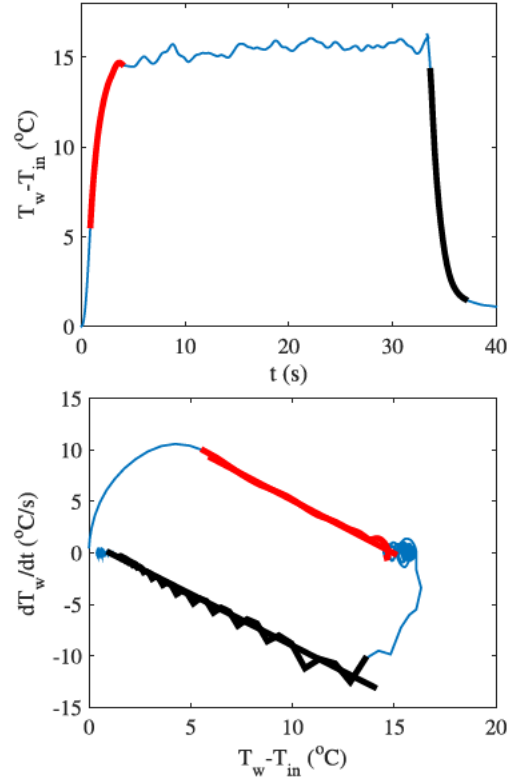


Fig. 21. Schema of the t_c calculus: an exponential evolution is assumed, and so a linear part of $\frac{dT_w}{dt}$ versus $T_w - T_{in}$ with a slope $1/t_c$. Red part corresponds to the heating, and black part corresponds to the cooling

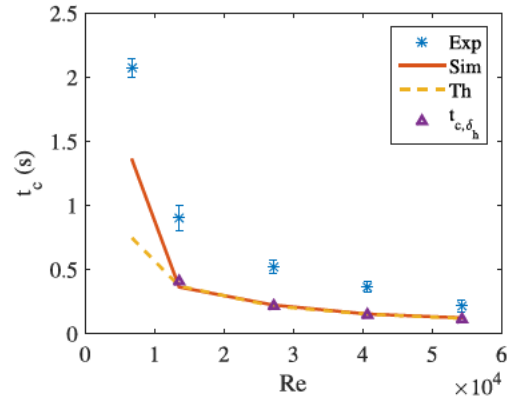


Fig. 22. Characteristic time t_c .

painting layer in the computational domain of the wall.

The characteristic time t_{c,δ_h} to establish the boundary layer based on the enthalpy δ_h is also plotted in Fig. 22. In the previous part, we showed that δ_h is characteristics of the viscous and buffer layers thicknesses near the wall, where the most part of the heat transfer takes place. Here, we verify that its establishment characteristic time t_{c,δ_h} is the same as the wall characteristic time of temperature variation t_c .

The transient convection (with either heating or cooling) only depends on the Reynolds number Re through the Nusselt number Nu . The wall temperature is scaled by the steady wall temperature, and the transient regime is characterized by a time scale decreasing with the Reynolds number. The characteristic time measured in the simulations agrees with the analytical result, however there is a

difference with the experiments. The boundary layer based on the enthalpy is characteristic of the heat transfer at the wall and establishes in the same time as the characteristic time of wall temperature variation.

7. Conclusions

Velocity and temperature profiles have been characterized in a semi annular geometry in steady and transient convection. In an angular sector of $\pi/2$ around the symmetry plane, the velocity and temperature profiles are the same as in an annular geometry. The semi annular geometry is therefore relevant to simulate the flow around a fuel rod in a nuclear core.

To compare the velocity profile in the semi annulus symmetry plane with the results in an annulus, we defined an equivalent flow rate for the 2 geometries with identical inner and outer radii. Since side walls induce additional friction, the flow rate in an equivalent annulus is 2.2 times that in the semi annulus. With this equivalence, the velocity profile and the wall shear stress are in good agreement with the log law proposed by Kaneda et al. [10]. In an angular sector of $\pi/2$ around the symmetry plane, the velocity profile and wall shear stress remain the same as in the symmetry plane. Near the side walls, the mean velocity and wall shear stress rapidly decrease.

In steady convection, the bulk temperature is constant along the 20 cm of the heated test section and the heat transfer is established after 10 cm from the inlet. The liquid temperature scaled by the friction temperature is well modeled by a log law. The relation established between the Nusselt number Nu and the friction velocity u_i^* is valid in the whole cross section. Two characteristic thermal boundary layer thicknesses are defined: $\delta_{99\%}$ corresponds to the upper limit of validity of the log law, where the liquid temperature reaches the bulk temperature and where the radial heat transfer is close to zero. δ_h is a thickness based on the enthalpy flux and it is limited to the viscous and buffer layers near the wall where most of the heat transfer takes place.

Transient convection tests were performed with a square power generation. The characteristic time of the transient decreases when the Nusselt number increases. The results of the numerical simulations are well fitted by an analytical solution. The wall heat transfer and the evolution of the liquid temperature near the wall have the same self similar evolution, which can be easily modeled. This result is of great interest for the study of the onset of nucleate boiling on a wall with a transient heating. It gives the time evolutions of the wall temperature and thermal boundary layer thickness which are required to determine the onset of nucleate boiling.

Appendix

The wall to fluid heat flux can be deduced from the wall energy balance:

$$\phi_w = \phi_{gen} - \rho_w C_{pw} \frac{dT_w}{dt} e_w \quad (22)$$

The heat flux and the wall temperature can be expressed in function of T_i , which leads to:

$$\lambda \frac{\partial T_i}{\partial y} \Big|_w = \phi_{gen} - \rho_w C_{pw} \frac{\partial T_i}{\partial t} \Big|_w e_w \quad (23)$$

Writing the difference between the steady and transient temperature distributions $\Delta T(y,t) = T_i(y,t) - T_{i,stat}(y)$, eq. (23) becomes:

$$\lambda \frac{\partial T_{i,stat}}{\partial y} \Big|_w + \lambda \frac{\partial \Delta T}{\partial y} \Big|_w = \phi_{gen} + \rho_w C_{pw} \frac{\partial \Delta T}{\partial t} \Big|_w e_w \quad (24)$$

In steady state condition, the wall to fluid heat flux reduces to:

$$\lambda \frac{\partial T_{i,stat}}{\partial y} \Big|_w = \phi_{gen} \quad (25)$$

Then, using eqs. (24) and (25), the equation with ΔT becomes:

$$\lambda \frac{\partial \Delta T}{\partial y} \Big|_w = \rho_w C_{pw} \frac{\partial \Delta T}{\partial t} \Big|_w e_w \quad (26)$$

Assuming that ΔT is the product of a space and a time function, i.e. $\Delta T = f(y)g(t)$, allows to write:

$$\lambda f'(0)g(t) = \rho_w C_{pw} f(0) \dot{g}(t) e_w \quad (27)$$

It leads to $g(t) = e^{-\frac{t}{t_c}}$ with:

$$t_c = \frac{\rho_w C_{pw} e_w f(0)}{\lambda f'(0)} \quad (28)$$

With the initial condition at $t = 0$ on the temperature and the heat flux, and assuming a constant bulk temperature T_b :

$$\Delta T(y = 0, t = 0) = f(0) = T_{w,stat} - T_b \quad (29)$$

$$\Delta T'(x = 0, t = 0) = f'(0) = T_{w,stat}' - \frac{\Phi_{gen}}{\lambda} \quad (30)$$

we finally find the expression for t_c :

$$t_c = \frac{\rho_w C_{pw} e_w}{\rho C_p} \frac{D_h^2}{D_h} \frac{1}{\alpha} \frac{1}{Nu_{stat}} \quad (31)$$

Actually, ΔT should be a sum of space and time functions product i.e. $\Delta T = \sum f_n(y) e^{-\frac{t}{t_{c,n}}}$. However, the evolution of ΔT in the simulation is only one exponential evolution, so we keep this form for the analytical model of the time constant.

References

- [1] Visentini R, Colin C, Ruyer P. Experimental investigation of heat transfer in transient boiling. *Exp. Therm. Fluid. Sci.* 2014;55:95–105.
- [2] Sparrow E, Chen T, Jonsson V. Laminar flow and pressure drop in internally finned annular ducts. *Int. J. Heat Mass Transf.* 1964;7(5):583–5.
- [3] Soliman H. Laminar heat transfer in annular sector ducts. *J. Heat Transf.* 1987;109(1):247–9.
- [4] Ben-Ali T, Soliman H, Zariffah E. Further results for laminar heat transfer in annular sector and circular sector ducts. *J. Heat Transf.* 1989;111(4):1090–3.
- [5] Tao W-Q, Lu S-S, Kang HJ, Lin MJ. Experimental study on developing and fully developed fluid flow and heat transfer in annular-sector ducts. *J. Enhanc. Heat Transf.* 2000;7(1):51–60.
- [6] Li Z-Y, Hung T-C, Tao W-Q. Numerical simulation of fully developed turbulent flow and heat transfer in annular-sector ducts. *Heat Mass Transf.* 2002;38:369–77.
- [7] Kang S, Patil B, Zarate J, Roy R. Isothermal and heated turbulent upflow in a vertical annular channel - part I. Experimental measurements. *Int. J. Heat Mass Transf.* 2001;44(6):1171–84.
- [8] Hasan A, Roy R, Kalra S. Heat transfer measurements in turbulent liquid flow through a vertical annular channel. *J. Heat Transf.* 1990;112(1):247–50.
- [9] Rehme K. Turbulent flow in smooth concentric annuli with small radius ratios. *J. Fluid Mech.* 1974;64:263–88.
- [10] Kaneda M, Yu B, Ozoe H, Churchill SW. The characteristics of turbulent flow and convection in concentric circular annuli. Part I: flow. *Int. J. Heat Mass Transf.* 2003;46(26):5045–57.
- [11] Visentini R. Étude expérimentale des transferts thermiques en ébullition transitoire. 2012. Ph.D. thesis, <http://ethesis.inp-toulouse.fr/archive/00002037/>.
- [12] Carslaw HS, Jaeger JC. *Conduction of heat in solids*. second ed. Oxford: Clarendon Press; 1959.
- [13] Dittus F, Boelter L. Heat transfer in automobile radiators of the tubular type. *Publ. Eng.* 1930;2(13):443.